Electronic Supplementary Material (ESI) for ChemComm.

# Supporting Information

## Contents

# S1- Synthesis

General: All reagents were commercially available and used as received (iron(II) perchlorate was handled carefully and in small amounts to avoid any potential explosions).

Synthesis of N-thiophenylidene-4H-1,2,4-triazol-4-amine (thtrz). 4-amino-1,2,4-triazole (1.5 g, 17.5 mmol) and thiophen-2-aldehyde (2.47 g, 21.9 mmol) was dissolved in 50 ml EtOH along with 4 drops of concentrated $H_2SO_4$. The solution was refluxed and stirred for 5 hours. With cooling to room temperature a white precipitate formed which was washed with cold water followed by ethanol. The crude product was recrystallised from ethanol (**Mw** 177.23; **Yield** 2.4 g (70 %); **$^1$H-NMR (200 MHz, MeOD-*$d_4$*, *δ*/ppm)**: 9.17 (s, 1H), 9.05 (s, 2H), 7.85 (d, $3J_{HH}$ = 5 Hz, 1H), 7.72 (d, $3J_{HH}$ = 3.6 Hz, 1H), 7.23 (t, $^3J_{HH}$ = 4.8 Hz, 1H); **ESI-MS** found M+H peak at m/z 178.80; **IR (solid, *ν*/cm$^{-1}$):** 3087 (m), 2963 (w), 1612 (m), 1595 (m), 1524 (s), 1505 (s), 1462 (w), 1431 (m), 1344 (m), 1305 (m), 1222 (m), 1170 (m), 1059 (s), 1024 (w), 969 (w), 941 (w), 863 (w), 841 (w), 801 (m), 1024 (s), 716 (m), 703 (m), 694 (m), 624 (m), 600 (w).

Synthesis of $[Fe(thtrz)_2Pd(CN)_4]\cdot(EtOH,H_2O)$. Crystals were grown by vial in vial slow diffusion. Powders of Thtrz (26.4 mg, 0.049 mmol) and $KPd(CN)_4$ (5.6 mg, 0.019 mmol) were placed at the base of a small vial. $Fe(ClO_4)_2\cdot 6(H_2O)$ (5.0 mg, 0.019 mmol) was placed at the base of a large vial. The small vial was placed inside the large vial and both carefully filled with 50:50 ethanol:water mixture being careful to fill vials without disturbing the reactants. The components were allowed to diffuse over a period of 2 weeks to form bright yellow square plates. **IR(cm$^{-1}$)** 3615 (w), 3569 (w), 3400 (sh), 3124 (m), 2168 (s), 1636 (sw), 1612 (m), 1597 (m), 1530 (m), 1513 (m), 1435 (s),1392(m), 1344(sh), 1310 (m), 1256 (w), 1225 (sh), 1173 (m), 1121 (m), 1108 (w), 1086 (w), 1059 (s), 1021 (w), 1004 (w), 968 (m), 953 (m), 862 (m), 849 (m), 802 (m), 717 (s), 621 (s), 604 (m), 419 (s).

## S2- Single Crystal X-ray Diffraction

Single-crystal diffraction data were collected at 180 and 260 K on two separate crystals using a Bruker APEX diffractometer equipped with a rotating anode ($\lambda$ = 0.7017 Å) and an Oxford Cryosystems nitrogen gas open flow cryostat. The crystals show non-merohedral twinning intrinsic to the thin stacked plate-like crystal morphology. Data for both twin components were indexed and integrated within the APEX software suite.[1] Empirical absorption corrections were carried out within TWINABS.

Single-crystal data was collected at 100 K on MX-2 at the Australian Synchrotron (λ = 0.71073 Å). Data were collected using the Blue Ice software.[2] Initial data processing was carried out using the XDS package.[3]

Structural solution for the three structures was completed with SHELXS-97 and refined using SHELXL-97 within the X-SEED user interface.[4-6] All atoms were refined anisotropically and hydrogen atoms were fixed using the riding model. Several carbon and sulfur atoms were split between two positions (50% occupancy), the sulfur atoms were refined anisotropically and the carbon atoms isotropically. One solvent ethanol and water molecule are located in the asymmetric unit; the oxygen atoms for each were only modeled. O1 refers to the water molecule and O2A and O2B are disordered oxygen atoms of the ethanol molecule. The crystal collected at 100 K was a very thin plate and resulted in large satellite peaks either side of the heavy metal atoms, these peaks were included in the structural solution (10% occupancy) to assist with refinement (Figure S3). The inherent twinning of these crystals and the solvent disorder in this porous material accounts for the R-factors in the vicinity of 5-10 % which by some accounts may be considered high for molecular materials but are within a very acceptable range for porous materials of this type.

A summary of the crystallographic and refinement details are located in Table S1 and relevant structural parameters are in Table S2. ORTEP representations for the three structures are shown in Figures S1-3. CCDC reference numbers 963504-6 for 100, 180 and 260 K structures, respectively.

An overlay of structural data at 260 and 180 K and 180 and 100 K, using Mercury,[7] is shown in Figure S4, highlighting that the greatest changes in ligand position occur at the site of spin crossover transition (i.e., $\mathbf{L}_{\mathbf{Fe2}}$ followed by $\mathbf{L}_{\mathbf{Fe1}}$ with cooling from 260 to 180 to 100 K).

A structural representation depicting the 2-D [FePd(CN)$_4$] layers is shown in Figure S5.

The structural distinctions between thtrz ligands have a striking effect on the spacing between adjacent ligands within the interlayer area. This difference generates alternating areas of dense complementary hydrogen-bonding containing all of the S-atoms, and larger void areas which are filled with ethanol and water molecules (Figure S6). Despite the affinity of sulfur atoms to interact,[8] there do not appear to be any S…S contacts. Alternating, offset dual-pore space motifs have been seen in Hofmann materials previously, where pyridyl binding groups were utilized.[9] Here, the use of a 1,2,4-triazole binding group promotes this arrangement further due to the availability of the unbound 2-nitrogen atom of the 1,2,4-triazole group for complementary ligand interactions.

The 2-D layers stack such that the thtrz ligands from adjacent layers inter-digitate and align in an eclipsed face-to-face fashion to form an array of interlayer $\pi$-interactions. This $\pi$-stacking network generates a pseudo-3-D character in the material – a platform that has previously been exploited to explore host-guest magneto-synergistic effects.[10,11] The guest molecules, comprised of a mixture of ethanol and water, reside in small pockets within the interlayer space (Figure S7). The water molecules are located in close proximity to the [FePd(CN)$_4$] layers (ca. 2.4 Å) and are approximately centrally disposed above the center of a $Fe_2Pd_2(CN)_4$ rhombus. These water molecules act as both a donor and acceptor in a chain of hydrogen bonding interactions between aromatic C(H) groups of the triazole of $\mathbf{L_{Fe1}}$ and the unbound N atom of the triazole of $\mathbf{L_{Fe2}}$, respectively. The ethanol molecules are located further from the [FePd(CN)$_4$] layers and participate in hydrogen-bonding interactions with the thiophene ring.

Lastly of significance, we find that within the IP region the HS and LS iron(II) sites are distributed within each [Fe$^{II}$Pd$^{II}$(CN)4] grid in alternating 1-D ribbons (Fig. S7) resulting in an undulating wave-like layer distortion. This differs from the more intuitive checkerboard arrangement of HS and LS sites within a 2-D grid usually observed in SCO 2-D layered structures. The HS and LS arrangement is propagated throughout the lattice in alternating 2-D planes due to the offset alignment of equivalent iron(II) sites in consecutive parallel grids (Fig. S7).

# **Table S1:** Crystallographic data summary

| Collection Temperature | **260 K** | **180 K** | **100 K** |
|---|---|---|---|
| Formula, FW / gmol$^{-1}$ | $C_{18}H_{12}FeN_{12}PdS_2.(H_2O, C_2H_6O)$<br>686.85 | | |
| Crystal system | Triclinic | Triclinic | Triclinic |
| Space group | *P-1* | *P-1* | *P-1* |
| $a$ / Å | 7.4566(11) | 7.2333(15) | 7.0850(14) |
| $b$ / Å | 13.554(3) | 13.404(3) | 13.334(3) |
| $c$ / Å | 14.747(3) | 14.527(3) | 14.383(3) |
| $\alpha$ / ° | 69.852(9) | 69.130(3) | 110.33(3) |
| $\beta$ / ° | 90.053(8) | 90.027(3) | 90.02(3) |
| $\gamma$ / ° | 74.024(9) | 74.359(3) | 105.40(3) |
| $V$ / Å$^3$ | 1337.6(4) | 1260.0(4) | 1221.9(4) |
| $\delta_{calc}$ / Mgm$^{-3}$ | 1.626 | 1.726 | 1.780 |
| $\mu$ / mm$^{-1}$ | 1.410 | 1.497 | 1.543 |
| data/restraints/parameters | 5016/24/375 | 6095/12/341 | 5684/42/388 |
| $R(F)$ $\{I>\sigma(I)$,all$\}^{(a)}$ | 0.0659{0.0956} | 0.0766{0.0988} | 0.0982{0.1032} |
| $R_w(F^2)$ $\{I>2\sigma(I)$, all$\}^{(b)}$ | 0.1684{0.2035} | 0.2065{0.2249} | 0.2596{0.2632} |
| GoF | 1.068 | 1.088 | 1.112 |

**Table S2.** Single crystal parameters

| | **260 K** | **180 K** | **100 K** |
|---|---|---|---|
| $d_{<\mathrm{Fe(1)-N}>}$ / Å[a] | 2.15(4) | 2.15(3) | 1.95(4) |
| $\mathrm{d}_{<\mathrm{Fe(2)-N}>}$ / Å[a] | 2.16(6) | 1.95(1) | 1.94(4) |
| $\Sigma_{<\mathrm{N-Fe(1)-N}>}$ / ° [b] | 11.3 | 21.2 | 9.2 |
| $\Sigma_{<\mathrm{N-Fe(2)-N}>}$ / ° [b] | 5.4 | 1.2 | 4.4 |
| Fe(1)-N-C(Pd) /° | 168.3, 167.6 | 164.8, 164.6 | 172.5, 172.4 |
| Fe(2)-N-C(Pd) /° | 176.1, 177.2 | 179.2, 178.3 | 177.9, 178.2 |
| Fe(1)-N-N(trz)/ ° (**A**) | 131.3 | 130.75 | 125.07 |
| Fe(2)-N-N(trz)/ ° (**B**) | 121.3 | 122.2 | 121.81 |
| **Hydrogen bonding interactions** | | | |
| N(6)…C(12)H / Å | 3.846(2) | 3.755(4) | 3.864(2) |
| N(12)…C(6)H / Å | 3.552(2) | 3.395(2) | 3.433(2) |
| S(1)…C(18)H / Å | 3.607(3) | 3.619(2) | 3.511(2) |
| N(10)…O(1)H / Å | 2.816(2) | 2.786(2) | 2.805(3) |
| O(1)H…C(5) / Å | 3.865(2) | 3.742(3) | 3.491(2) |
| O2(Et)…C9(H) / Å | 3.548(2) | 3.479(2) | 3.436(3) |
| O2(Et)…C14(H) / Å | 3.613(2) | 3.529(3) | 3.524(2) |

[a]Average Fe-N bond distance, [b]Octahedral distortion parameter calculated by sum of $|90-\theta|$ for the twelve N-Fe-N angles in the octahedron.[12] **A** and **B**: angle defined in manuscript.

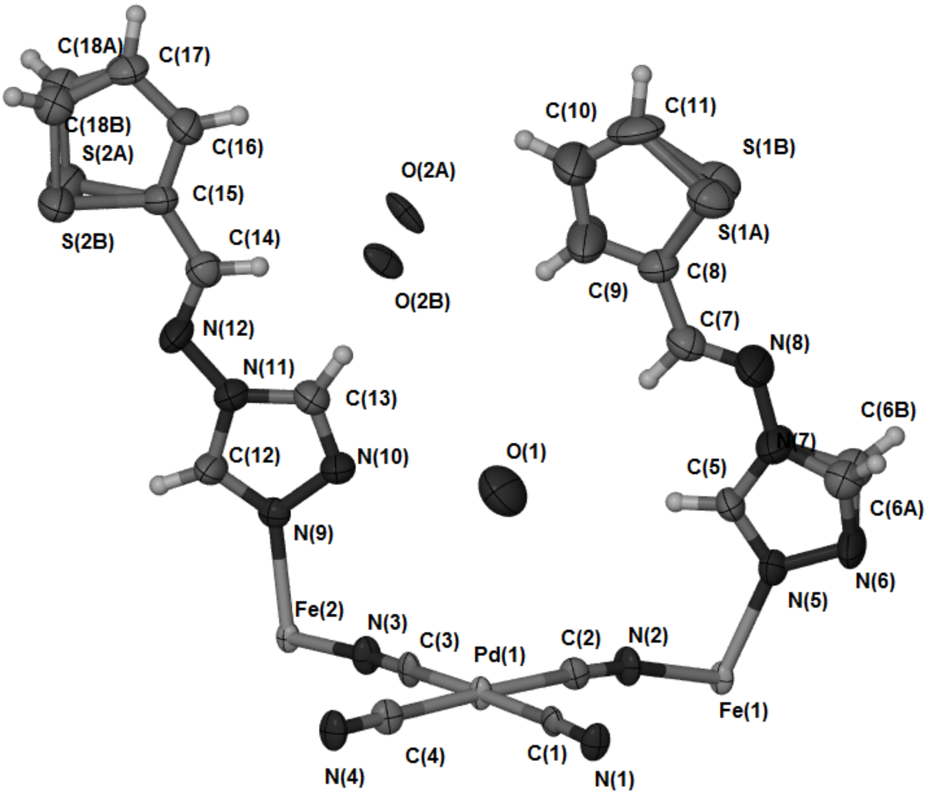

**Figure S1**: ORTEP representation (50%) of **1.(EtOH,H$_2$O)** at 260 K.

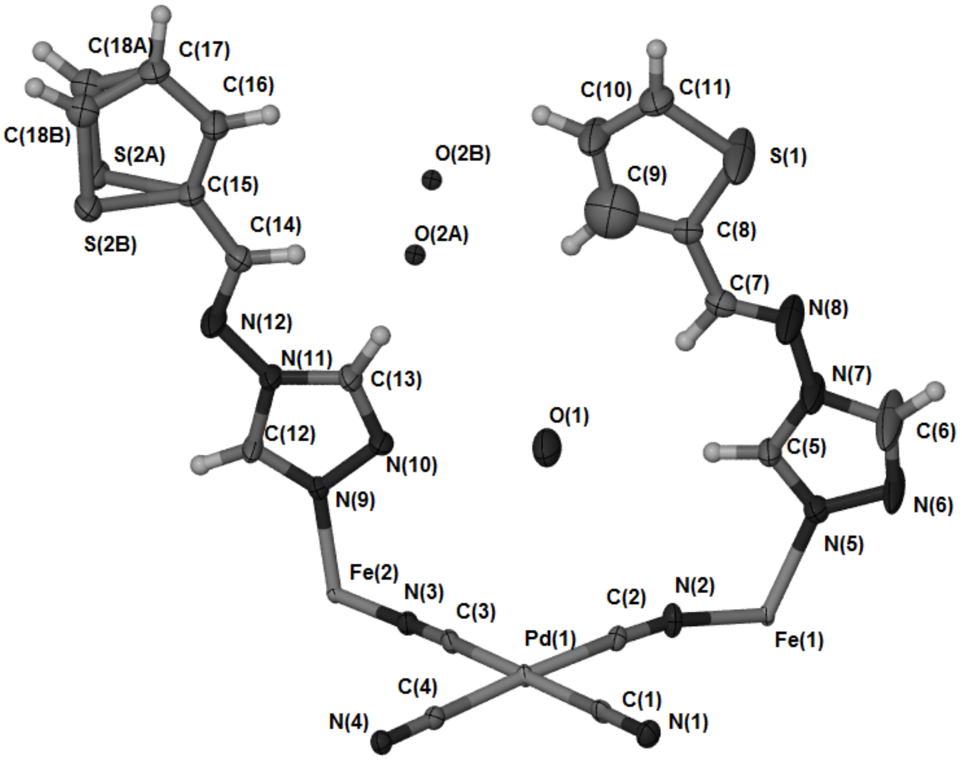

**Figure S2**: ORTEP representation (50%) of **1.(EtOH,H$_2$O)** at 180 K.

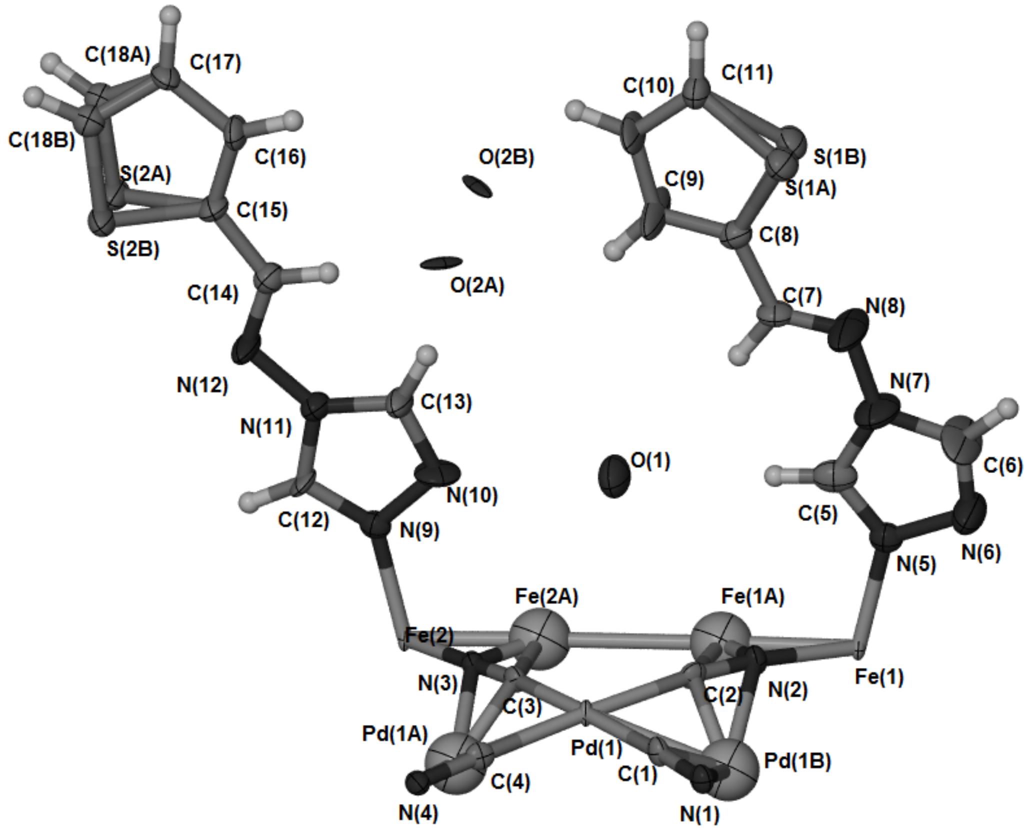

**Figure S3**: ORTEP representation (50%) of **1.(EtOH,$H_2O$)** at 100 K.

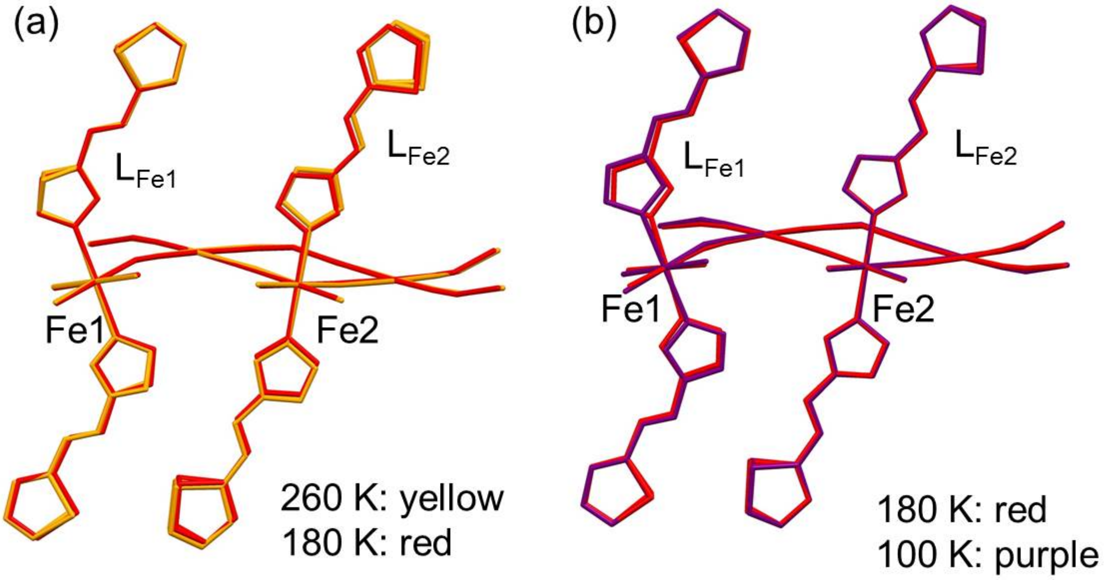

**Figure S4**: Mercury structural overlay of **1.(EtOH,$H_2O$)** at (a) 260 K and 180 K and (b) 180 K and 100 K.

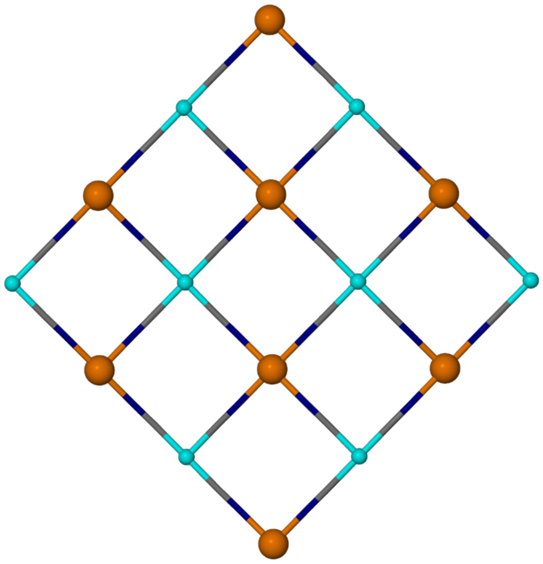

**Figure S5**: Structural representation highlighting the connectivity of one [$FePd(CN)_4$] grid lying in the *ac*-plane ($Fe^{II}$ sites yellow spheres, Pd sites green spheres).

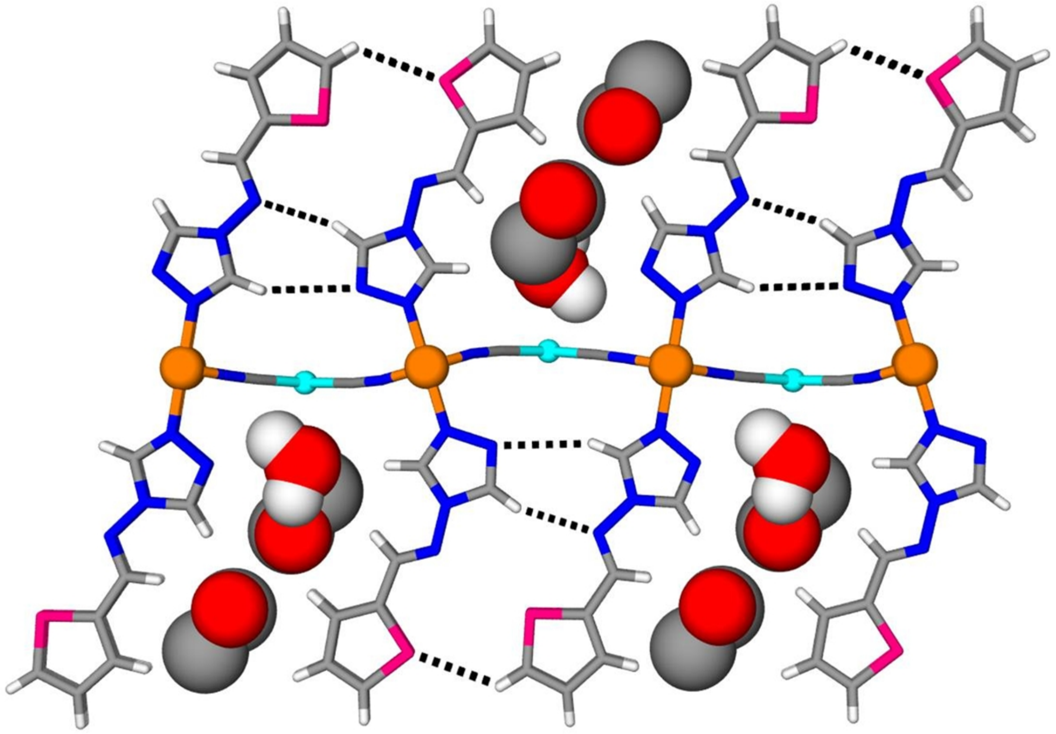

**Figure S6**: Structural representation showing solvent location (space-filling) and hydrogen bonding interactions (---).

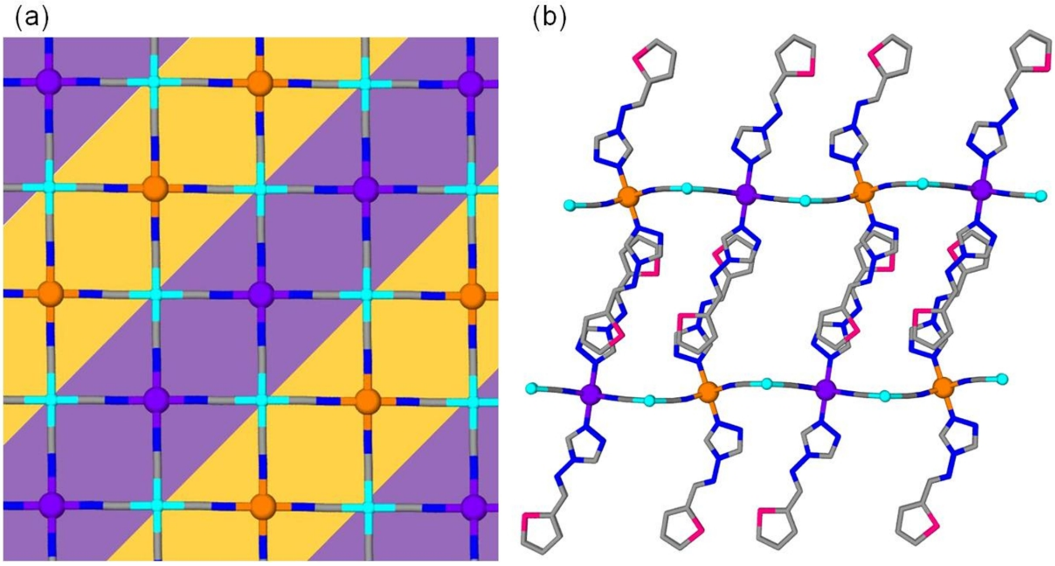

**Figure S7:** (a) Representation of (a) a single [$Fe^{II}Pd^{II}(CN)_4$] grid and (b) two layers of 1·(EtOH,$H_2O$), highlighting the arrangement of HS and LS iron(II) sites at IP temperatures.

# S3 –Synchrotron-Based Powder X-ray Diffraction

Polycrystalline samples of **1.(EtOH,$H_2O$)** were ground as a slurry and loaded into a quartz capillary (0.7 mm diameter) and sealed to prevent solvent loss. The X-rays (17.03 keV, 0.72808 Å) available at the 17-BM beamline at the Advanced Photon Source at Argonne National Laboratory were used in combination with a Perkin Elmer area detector with a Carbon window to record diffraction patterns. The sample temperature was controlled using an Oxford Cryosystems open flow cryostat, and the data were collected in 20 s exposures upon continuous ramping over the range 300 – 100 K, at 120 K $h^{-1}$. This corresponds to the collection of diffraction images at 2 K intervals. The raw images were processed using Fit-2D.[13,14] $LaB_6$ was used as a standard. Le Bail analyses of the diffraction data were performed within TOPAS.[15] Figure S8 shows a typical LeBail fit. Figures S9-12 show the *a*, *b*, *c*-axis and volume evolution *versus* temperature. The *a*- and *c*-axes define the $[Fe(Pd(CN)_4)]$ plane and show abrupt changes with temperature owing to the coordinative bond propagation of spin switching information in these directions. On the other hand, the *b*-axis defines the interlayer spacing/spacing between layers and shows a more subtle change with temperature, reflecting the more flexible through space propagation of spin switching in this direction occurring *via* intermolecular interactions.

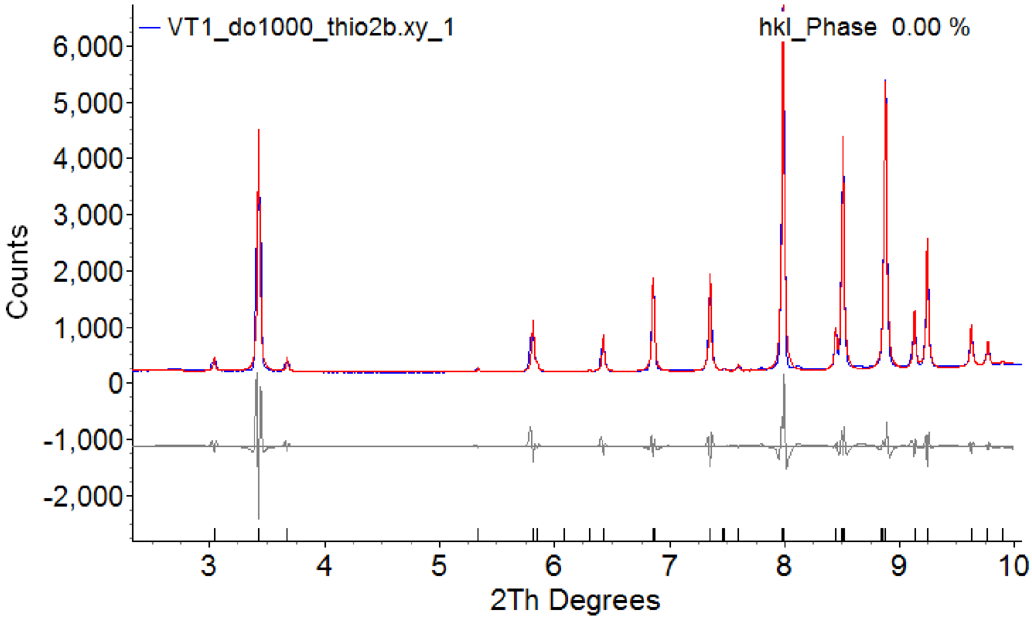

**Figure S8**: Representative Le Bail refinement for **1.(EtOH,$H_2O$)**.

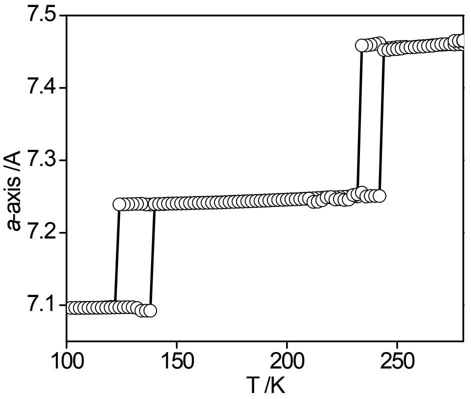

**Figure S9**: Evolution of the *a*-axis parameter versus temperature for **1.(EtOH,$H_2O$)**.

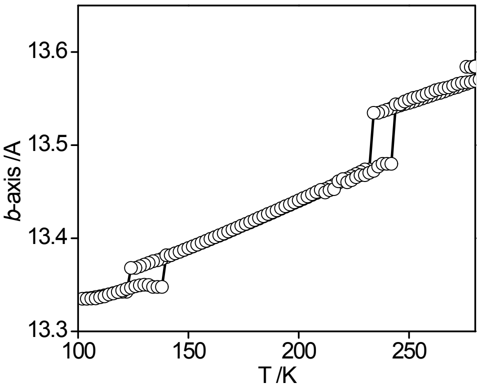

**Figure S10**: Evolution of the *b*-axis parameter versus temperature for **1.(EtOH,$H_2O$)**.

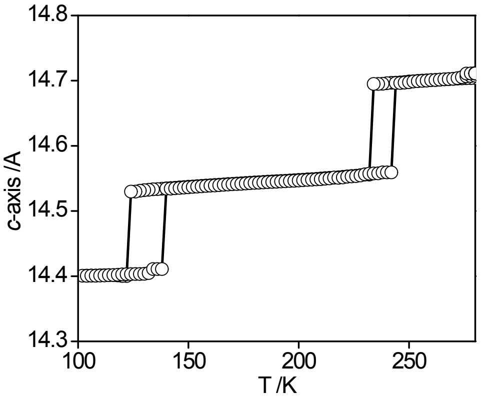

**Figure S11**: Evolution of the *c*-axis parameter versus temperature for **1.(EtOH,$H_2O$)**.

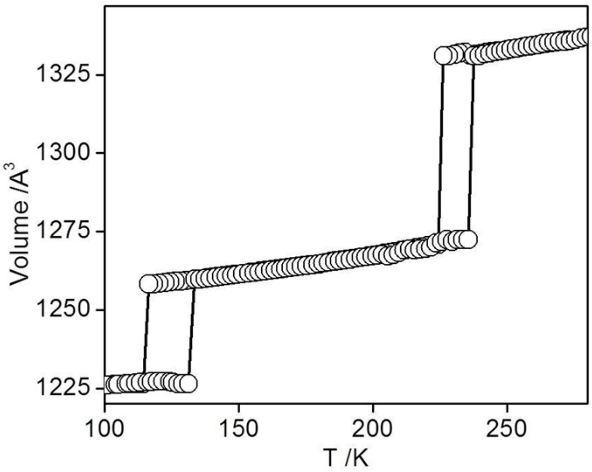

**Figure S12**: Evolution of the unit cell volume versus temperature for **1.(EtOH,$H_2O$)**.

# S4 – Magnetic Susceptibility Measurements

Magnetic susceptibility measurements were made using a Quantum Design Versalab instrument with the Vibrating Sample Magnetometer (VSM) operating under a field of 0.3 T. All measurements were performed on a bulk sample of crystal isolated kept wet under a thin layer of solvent to prevent desolvation.

As recent studies have shown the importance of measuring samples under a variety of conditions[16] we carried out experiments using both sweep and settle modes and at a range of rates (1, 1.5, 3, 4 Kmin$^{-1}$). An overlay of the magnetic data collected at a range of rates is shown in Figure S13 (we note that these measurements were each carried out on separate samples) where the main difference arises in the lower temperature hysteresis loop. The main variability in magnetic data was noted between different sample batches especially in the abrupt and complete nature of the transition, this is likely owing to the relative degrees of crystallinity and number of defects. Finally, multiple thermal cycles we carried out on samples to ensure constant magnetic response (Figure S14).

We note that the calorimetric and Mössbauer data on this material are important in providing further insight to this abrupt and hysteretic two-step SCO phenomenon and will be provided and detailed in a subsequent full paper.

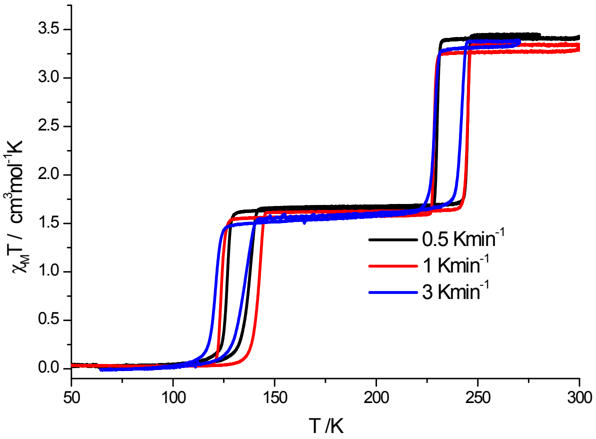

**Figure S13**: Rate dependency (carried out on separate samples)

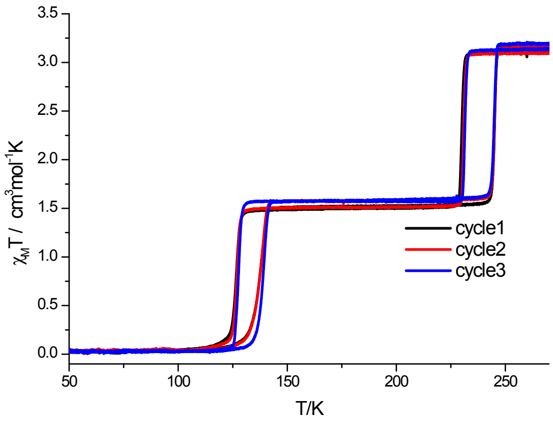

**Figure S14**: Thermal cycles on the one sample, highlighting no change in SCO character.

# S5 – References

(1) *APEX II Software Package* **2005**, *Bruker AXS Inc.*, Madison.

(2) McPhillips, T. M.; McPhillips, S. E.; Chiu, H. J.; Cohen, A. E.; Deacon, A. M.; Ellis, P. J.; Garman, E.; Gonzalez, A.; Sauter, N. K.; Phizackerley, R. P.; Soltis, S. M.; Kuhn, P. *J. Synchrotron Radiat.* **2002**, *9*, 401.

(3) Kabasch, W. J. *J. Appl. Crystallograph.* **1993**, *26*, 795.

(4) Bruker Analytical Instruments Inc.: Madison, Wisconsin, USA, 1995.

(5) Bruker Analytical Instruments Inc.: Madison, Wisconsin, USA, 1997.

(6) Barbour, L. J. University of Stellenbosch, South Africa, 1999.

(7) Martinez, V.; Castillo, Z. A.; Munoz, M. C.; Gaspar, A. B.; Etrillard, C.; Letard, J.-F.; Terekhov, S. A.; Bukin, G. V.; Levchenko, G.; Real, J. A. *Eur. J. Inorg. Chem.* **2013**.

(8) Constable, E. C.; Housecroft, C. E.; Neuburger, M.; Price, J. R.; Zampese, J. A. *CrystEngComm* **2010**, *12*, 2928.

(9) Martínez, V.; Gaspar, A. B.; Muñoz, M. C.; Bukin, G. V.; Levchenko, G.; Real, J. A. *Chem. Eur. J.* **2009**, *15*, 10960.

(10) Halder, G. J.; Kepert, C. J.; Moubaraki, B.; Murray, K. S.; Cashion, J. D. *Science* **2002**, *298*, 1762.

(11) Neville, S. M.; Moubaraki, B.; Murray, K. S.; Kepert, C. J. *Angew. Chem. Int. Ed.* **2007**, *46*, 2059.

(12) Guionneau, P.; Marchivie, M.; Bravic, G.; Létard, J.-F.; Chasseau, D. C. *Top. Curr. Chem.* **2004**, *234*, 97.

(13) Hammersley, A. P. *ESRF Internal Report* **1997**, ESRF97HA02T.

(14) Hammersley, A. P.; Svensson, S. O.; Hanfland, M.; Fitch, A. N.; Hausermann, D. *High-Pressure Res.* **1996**, *14*, 235.

(15) Gütlich, P.; Gaspar, A. B.; Garcia, Y. *Beilstein J. Org. Chem.* **2013**, *9*, 342.

(16) R. Kulmaczewski; J. Olguín; J. A. Kitchen; H. L. C. Feltham; G. N. L. Jameson; J. L. Tallon; Brooker, S. *J. Am. Chem. Soc.* **2014**, dx.doi.org/10.1021/ja411563x.